Research Article

Compact microring resonator based on ultralow-loss multimode silicon nitride waveguide

Shuai Cui,[a,b] Kaixiang Cao,[a,b] Zhao Pan,[a,b] Xiaoyan Gao,[a,b] Yuan Yu,[a,b,*] and Xinliang Zhang[a,b]

[a]Huazhong University of Science and Technology, School of Optical and Electronic Information, Wuhan National Laboratory for Optoelectronics, Wuhan, China

[b]Optics Valley Laboratory, Wuhan, China

Abstract. Silicon nitride (Si_3N_4) waveguides with high confinement and low loss have been widely used in integrated nonlinear photonics. Indeed, state-of-the-art ultralow-loss Si_3N_4 waveguides are all fabricated using complex fabrication processes, and all of those reported that high Q microring resonators (MRRs) are fabricated in laboratories. We propose and demonstrate an ultralow-loss Si_3N_4 racetrack MRR by shaping the mode using a uniform multimode structure to reduce its overlap with the waveguide. The MRR is fabricated by the standard multi project wafer (MPW) foundry process. It consists of two multimode straight waveguides (MSWs) connected by two multimode waveguide bends (MWBs). In particular, the MWBs are based on modified Euler bends, and an MSW directional coupler is used to avoid higher-order mode excitation. In this way, although a multimode waveguide is used in the MRR, only the fundamental mode is excited and transmitted with ultralow loss. Meanwhile, thanks to the 180 deg Euler bend, a compact chip footprint of 2.226 mm perimeter with an effective radius as small as 195 μm and a waveguide width of 3 μm is achieved. Results show that based on the widely used MPW process, a propagation loss of only 3.3 dB/m and a mean intrinsic Q of around 10.8 million are achieved for the first time.

Keywords: silicon nitride; microring resonator; ultrahigh-Q factor.

Received Apr. 21, 2023; revised manuscript received Jun. 9, 2023; accepted for publication Jun. 19, 2023; published online Jul. 4, 2023.

1 Introduction

The past decades have witnessed dramatic progress in the development of photonic integrated circuits in silicon-on-insulator. Silicon (Si) has been the mainstream platform of integrated photonics,[1] with the key advantages including large-area substrates, and mature and high-yield complementary metal oxide semiconductor (CMOS)-compatible fabrication. Tremendous effort, such as sophisticated fabrication processes and a highly multimode structure, has been made to improve the Q-factor of Si photonic resonators.[2,3] However, the propagation loss still cannot be reduced sufficiently low. The main reason is the two-photon absorption of the telecommunication wavelengths has drastically restricted its applications to occasions requiring low propagation loss at high power, such as tunable lasers[4] and optical frequency combs.[5] To address this challenge, silicon

nitride (Si_3N_4) has emerged as an attractive CMOS-compatible alternative to integrated photonics.[6–9] The 5 eV bandgap of Si_3N_4 makes it transparent from ultraviolet to mid-infrared, and immune to two-photon absorption in the telecommunication band, which means it has very low propagation loss.[10] Combining with its high Kerr nonlinearity and weak Brillouin scattering, Si_3N_4 has become the material of choice, particularly for Kerr nonlinear photonics.[11] Because of these advantages, the Si_3N_4 waveguides have been proposed to be integrated with other active and passive optical components[12–17] to boost the performance of the device.

Several approaches have been proposed to achieve ultralow propagation loss in Si_3N_4 waveguides. A propagation loss as low as 3 dB/m or even lower than 0.1 dB/m[11,18–20] has been achieved using weak optical confinement waveguides, which are less sensitive to the rough sidewalls. However, the thin Si_3N_4 exhibits low optical confinement and thus suffers from exaggerated bending loss when the footprint is small. Therefore, to reduce the loss, the perimeter of the high Q

*Address all correspondence to Yuan Yu, yuan_yu@hust.edu.cn

resonators is pushed to 9.65[20] and 11.787 mm,[18] respectively. This significantly reduces the compactness and induces a small free spectral range (FSR), which is quite disadvantageous for applications requiring a large FSR, such as microwave photonics,[21] optical signal processing,[22] and sensing applications.[23] In parallel, low propagation loss in high-confinement waveguides is critical for chip-based nonlinear applications or compact photonic routing. A thick Si_3N_4 of ultralow loss has been fabricated by the photonic Damascene process via advanced CMOS. The silica (SiO_2) substrate is prepatterned and reflowed prior to Si_3N_4 deposition.[24] Very recently, a propagation loss as low as 1 dB/m has been achieved by introducing complex fabrication processes such as "preform reflow" and thermal anneal.[11,25–27] However, there are inherent limitations to these techniques. For example, if the chemical mechanical planarization polishing rates for the waveguide material and cladding are different, the dishing effect may occur, which may lead to significant structure distortion and top surface roughness.[10] Alternatively, Si_3N_4 waveguides can be fabricated using traditional subtractive processing methods, where the Si_3N_4 film is lithographically patterned.[19,28] A propagation loss as low as 2.6 dB/m or even lower is also achieved by introducing extra fabrication processes, such as multipass lithography, optimized etch recipe, surface smoothing technique, or thermal anneal.[10,19,28,29] However, one should note that these special fabrication techniques are not standard and are usually incompatible for foundries. Moreover, these complex fabrication approaches are not available generally for different material platforms. Therefore, it is still significantly desired to achieve ultralow propagation loss of Si_3N_4 waveguides using the regular standard fabrication processes.

In this work, we propose and demonstrate an ultrahigh Q Si_3N_4 racetrack resonator based on a uniform multimode Si_3N_4 waveguide, even without any special fabrication process. The multimode waveguide, which refers to the waveguide width that is far beyond the single-mode regime, is used to reduce the contact between the optical field and the rough sidewall, thus reducing the scattering loss of the optical waveguide. The microring resonator (MRR) consists of two adiabatic Euler bends and two multimode straight waveguides (MSWs). Multimode directional couplers (DCs) are used to achieve the adiabatic propagation of the fundamental mode and suppress the excitation of higher-order modes in the racetrack. With the help of Euler bends and a DC, a compact footprint resonator with a large FSR, ultralow loss, and low intermode coupling is achieved. The high-Q Si_3N_4 resonator is fabricated with simple standard 800-nm-Si_3N_4 multi project wafer (MPW) foundry processes. Notably, the racetrack Si_3N_4 resonator is made of a 3.0-μm-wide uniform waveguide, and the perimeter is only 2.226 mm, corresponding to an FSR of ~65.0 GHz. Compared with previously reported results,[30] the mean intrinsic Q of the MRR is increased by more than 5 times higher order and reached 10.8 million for the first time, and the corresponding propagation loss is estimated to be about 3.3 dB/m. Our method of using highly multimode structures to achieve ultralow propagation loss can be applied to other material platforms. It can potentially be applied to optical frequency combs, microwave photonic filters, and optoelectronic oscillators.

2 Device Design

Figures 1(a) and 1(b) show the three-dimensional (3D) and the top views of the designed ultrahigh Q racetrack resonator based on a uniform multimode Si_3N_4 waveguide. The racetrack MRR is composed of two MSWs and two multimode waveguide bends (MWBs) based on modified Euler bends. Although the waveguide width of the Euler bends is far beyond the single mode, the Euler bends can guarantee adiabatic transmission for the fundamental mode with low intermode cross talk, ultralow excess loss, and a compact footprint. No higher-order modes are excited in the MRR. A DC is used to couple the light from the bus waveguide to the MRR. Notably, the DC is realized using two MSWs with the same width. By controlling the coupling length and the coupling gap, the optical coupling only occurs for the fundamental mode, and higher-order mode excitation is suppressed.

Figure 2(a) shows the cross section of the Si_3N_4 waveguide, whose core width W_{co} is broadened to weaken the optical sidewalls' interaction and thus reduce the light scattering loss at the sidewalls significantly. The wafer is with an 800-nm-thick Si_3N_4 layer and a 4-μm-thick buried-oxide layer. A 3.3-μm-thick SiO_2 thin film is deposited on the top as the upper cladding. The interaction between the optical field and the rough sidewalls is responsible for distributing the scattering loss. Here, we use an n-w model to analyze the scattering loss, which provides a comprehensive analysis of the fundamental role played by the sensitivity of the effective index of the optical mode to waveguide width variations.[31] This approach enables an accurate description of practical optical waveguides and provides simple design rules for optimizing the waveguide geometry, thus reducing the scattering loss generated by rough sidewalls. According to the Si_3N_4 design rules of LIGENTEC AN800 Technology (LAT), the propagation loss is ~20 dB/m for the standard Si_3N_4 waveguide with a cross section of 0.8 μm × 1.0 μm. The relationship between waveguide width and scattering loss can be predicted by the n-w model. From Fig. 2(b), it can be seen that when the standard deviation of the roughness σ and the correlation length (L_c) of the rough sidewalls are determined, the scattering loss decreases with the increase of waveguide core width W_{co}. This happens because when the waveguide core becomes wider, the optical field at the sidewalls of the waveguide becomes weaker. We can also see that when W_{co} is larger than 3 μm, the scattering loss is not very sensitive to the increase of W_{co}. Further, as the waveguide width increases, the MRR footprint will consequently increase.
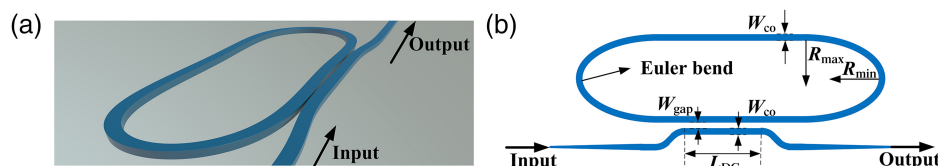
Fig. 1 Schematic diagram of the proposed compact ultrahigh-Q MRR. (a) 3D view and (b) top view.
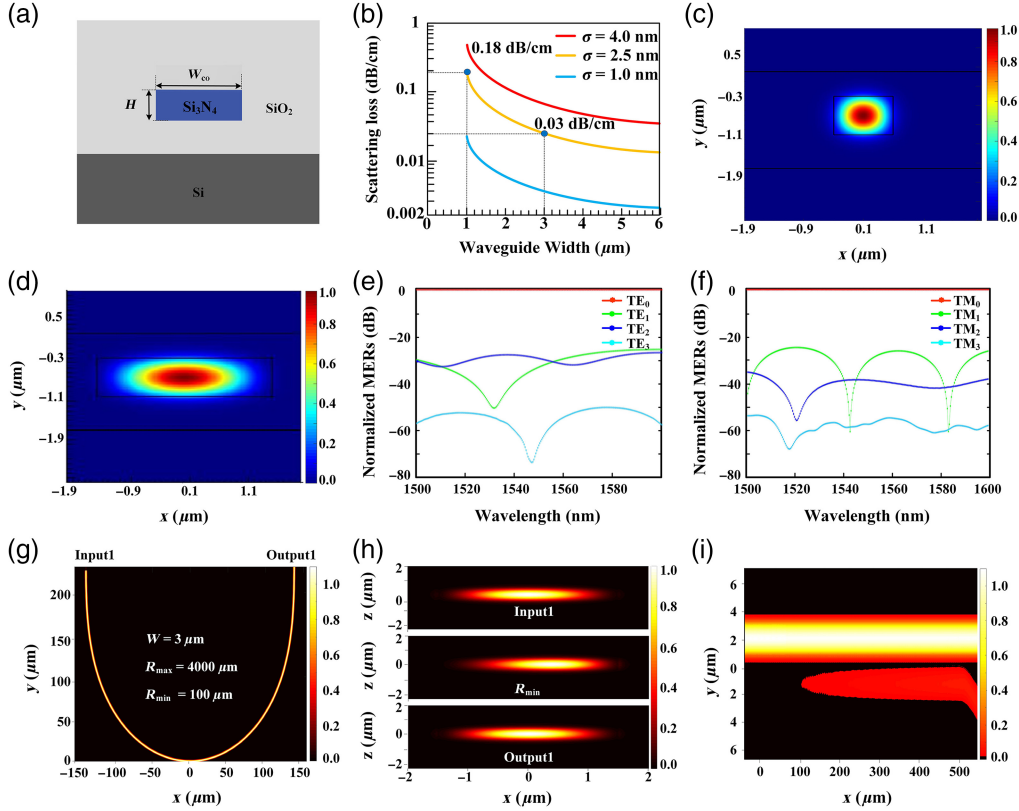
Fig. 2 Design of the compact ultrahigh-Q microracetrack resonator. (a) Cross section of the Si_3N_4 optical waveguide of the resonator; (b) relationship between the scattering loss and the waveguide core width based on n-w model; (c), (d) simulated mode profiles when the waveguide widths are 1 and 3 μm, respectively; (e), (f) calculated respective MERs of the higher-order TE modes excited by TE_0 mode and MERs of the higher-order TM modes excited by TM_0 mode, in the waveguide consisting of an input MSW, a 180 deg Euler MWB, and an output MSW, when $R_{min} = 100$ μm, $R_{max} = 4000$ μm; (g) simulated TE_0 mode propagation in the designed 180 deg Euler MWBs; (h) simulated TE_0 mode profile at the input (top), the quadrant MRR ($R = R_{min}$) (middle), and the output (bottom) of the 180 deg Euler MWBs; and (i) FDTD simulations of the light coupling in the MSW DC.

Therefore, to balance the bending radius and the waveguide loss, the waveguide width is designed to be 3 μm.

Figures 2(c)–2(d) show the mode profiles in the 1- and 3-μm wide waveguides, which are simulated by the finite-difference Eigenmode method provided by Lumerical MODE Solutions. We can clearly see that when the waveguide width is 3 μm, the contact between the TE_0 (TE = transverse electric) mode and the rough sidewalls is much less than when the waveguide width is 1 μm. Thus, the scattering loss caused by the rough sidewalls is significantly reduced. According to the n-w model shown in Fig. 2(b), the estimated scattering loss of the Si_3N_4 waveguide ($\sigma = 2.5$ nm and $L_c = 50$ nm) are 0.18 and 0.03 dB/cm when the waveguide widths are 1 and 3 μm, respectively. Therefore, the Q value of the MRR can be significantly boosted.

To ensure the fundamental mode to be transmitted in the ring adiabatically, the MWBs should be carefully designed to avoid exciting higher-order modes. To achieve high integration density as well as a large FSR, the MWBs with modified Euler bends are used in the MRR. The modified Euler curve means that the curvature varies linearly along the length of the curve and can provide a high degree of adiabaticity and compact footprint. The Euler bend is defined as[2]

$$\frac{d\theta}{dL} = \frac{1}{R} = AL + \frac{1}{R_{max}},$$ (1)

and

$$A = \left(\frac{1}{R_{min}} - \frac{1}{R_{max}}\right)/L_0,$$ (2)

where θ is the center angle corresponding to the unit length of the curve, L is the curve length, R is the curvature radius, A is a constant, L_0 is the length of the 90 deg Euler curve, and R_{max} and R_{min} are the maximal and the minimal radii of the curvature radius, respectively.

As shown in Fig. 1(b), the 180 deg bend comprisesf a pair of 90 deg Euler bends. Notably, the maximal radius R_{max} should be large enough to ensure negligible mode mismatch at the junction between the MSW and the MWBs, and R_{min} should be chosen to ensure adiabatic transmission. We simulate the mode field in the 3-μm-wide waveguide and find that the lowest four modes (TE_0, TE_1, TE_2, and TE_3) can all be well supported. Using the 3D finite-difference time-domain (FDTD) simulations (Lumerical

FDTD), we simulate and calculate the mode excitation ratios (MERs) of the higher-order modes at different R_{max} and R_{min}, and find that when $R_{max} = 4000\ \mu m$ and $R_{min} = 100\ \mu m$, the calculated MERs, such as TE_1, TE_2, and TE_3, are all below -25 dB in the broadband from 1500 to 1600 nm, as shown in Fig. 2(e). Therefore, the cross talk of the higher-order modes calculated in the MWR can be ignored. It should be noted that the waveguide height is $0.8\ \mu m$, which can also support transverse magnetic (TM) mode transmission. Therefore, we also calculate the MERs of higher-order TM modes excited by TM_0 mode, as shown in Fig. 2(f). The calculated MERs of TM_1, TM_2, and TM_3 excited by TM_0 mode are all below -20 dB in the broadband from 1500 to 1600 nm. Therefore, the cross talk of the higher-order modes of the TM mode can also be ignored.

Figure 2(g) shows the simulated light propagation field in the 180 deg Euler MWBs when $R_{max} = 4000\ \mu m$ and $R_{min} = 100\ \mu m$. The corresponding mode profile at the input, the quadrant MRR ($R = R_{min}$), and the output of the 180 deg Euler MWBs are shown in Fig. 2(h). It can be seen that almost no multimode interference is observed, which indicates that the designed Euler MWBs work very well. Meanwhile, the optical field is well confined in the Si_3N_4-core region and has little interaction with the sidewalls. For the designed MWBs, the effective radius of the ring R_{eff} is calculated to be only $195\ \mu m$. A Si_3N_4 multimode MRR with a constant large radius of $230\ \mu m$ is proposed with a cross section of $2\ \mu m \times 0.85\ \mu m$.[24] For this MRR, it is also difficult to reduce the bending radius due to intermode coupling. In contrast, the proposed racetrack resonator is made of a $3.0\text{-}\mu m$-wide uniform multimode waveguide, with an effective radius R_{eff} as small as $195\ \mu m$.

In addition, the DC-based multimode waveguides should also be carefully designed to ensure adiabatic coupling for the fundamental mode. To ensure sufficient coupling for the fundamental mode and avoid exciting the higher-order modes, the coupling length of the multimode DC of the MRR should be long enough, and the coupling gap should be sufficiently small. By choosing $w_{gap} = 0.8\ \mu m$ and the length of DC $L_{DC} = 400\ \mu m$, we can obtain the simulated light propagation in the multimode DC from the racetrack to the bus waveguide, as shown in Fig. 2(i). It can be seen that no higher-order modes are excited

in our designed multimode DC. It should be noted that the waveguide width W_{co} is far beyond the single-mode regime and can support multimode transmission in the optical waveguide.[32] When light propagates along the waveguide beyond the single-mode regime, higher-order modes can be excited and thus induce undesired mode-mismatching loss as well as intermode cross talk. Thanks to the designed adiabatic coupler and Euler bend, only the fundamental mode is excited and transmitted in our designed resonator.

To summarize, the adiabatic transmission process of TE_0 mode is as follows. First, the TE_0 mode is input into the bus waveguide, and the TE_0 mode is adiabatically coupled to the MRR by the specially designed multimode DC. Then, the TE_0 mode undergoes adiabatic transmission in the MWBs, and finally, the TE_0 mode is adiabatically coupled from the MRR back to the bus waveguide. In the designed MRR, the power cross-coupling ratio of the DC is 0.006, and the perimeter of the MRR is $2226\ \mu m$.

3 Device Fabrication and Measurement

Figure 3 shows the false color image of the fabricated compact ultrahigh Q racetrack resonator. All the devices in this work are fabricated by the MPW foundry (LIGENTEC, Switzerland) with the standard processes of deep ultra-violet (DUV) lithography. Figure 3(a) shows the global view of the resonator with a size of $0.27\ mm \times 0.98\ mm$. The microscopic images of the modified Euler bend, the adiabatic taper, and the DC are shown in Figs. 3(b)–3(d), respectively. Figure 4 shows the experimental setup for characterizing the Q factor of the fabricated ultrahigh Q Si_3N_4 racetrack resonator, which maps the bandwidth of the MRR from the optical domain to the electrical domain.[33] The optical carrier emitted by a tunable laser source (TLS, NKT Basik E15) is input into a phase modulator (PM, Covega Mach-40) via a polarization controller (PC1). Then the phase-modulated light is launched into an optical bandpass filter (OBPF). One of the first-order sidebands of the modulated signal is eliminated by the OBPF and then a single sideband (SSB) signal can be obtained correspondingly. The remaining sidebands of the generated SSB signal are used to scan the resonant notch to obtain the transmission spectrum

(a)

(b)

(c)

(d)
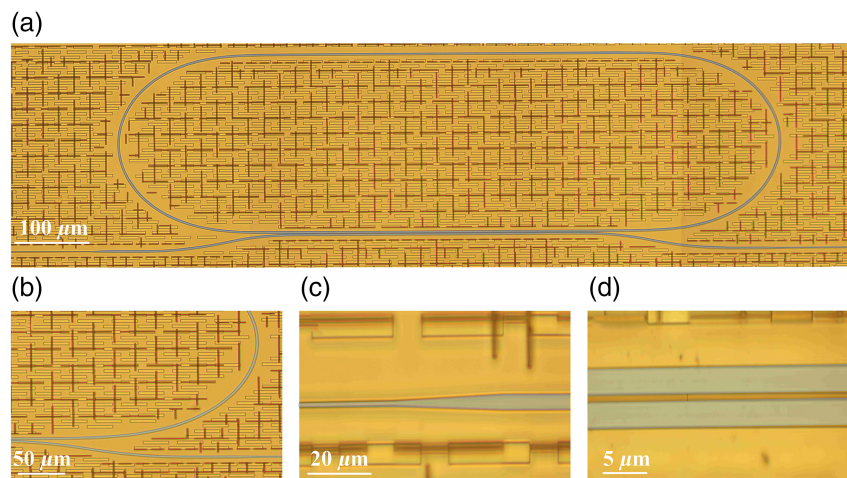
Fig. 3 False color images of the fabricated ultrahigh-Q Si_3N_4 racetrack resonator. (a) Global view of the fabricated device; (b) modified Euler bend; (c) adiabatic taper; and (d) coupling waveguides of DC.
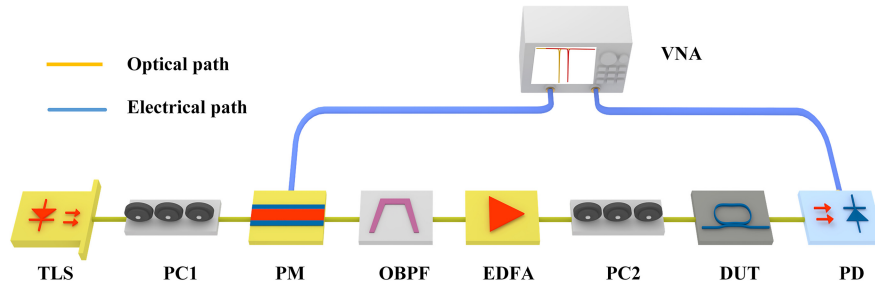
Fig. 4 Experimental setup for characterizing the Q factor of the compact ultrahigh-Q Si$_3$N$_4$ race-track resonator based on VNA.

of the racetrack microring. Then the light is amplified by an erbium-doped fiber amplifier and coupled into the chip via PC2, which is used to adjust the state of polarization (SOP) of the light to the chip. A pair of tapered optical fibers (OMT-APC-TJ-1M), which are fixed by flip-top fiber optic clamps (OMFG06, OMTOOLs), are used to couple the light into and out of the device under test. Then the SSB signal is launched into the chip. After being filtered by MRR, the output signal is routed to a high-speed photodetector (PD, SHF AG-Berlin) with a bandwidth of 40 GHz. Finally, a microwave photonic notch filter (MPNF) is obtained, and the transmission of the ultra-high Q resonator is mapped to the transmission of the MPNF. Therefore, the transmission of the ultrahigh Q resonator can be measured by a vector network analyzer (VNA, Anritsu MS4647B) precisely.

In this section, we characterize the FSR and Q factor of our designed and fabricated ultrahigh-Q MRR. Since precise frequency calibration is required to measure the FSRs, we adjust the wavelength of the TLS carefully to expand the measurement

range to several FSRs of the MRR (see Appendix). From Fig. 5(a), it can be seen that both the TE and TM modes exist in an FSR. This is because the thickness of the Si$_3$N$_4$ waveguide is 0.8 μm, which also supports TM mode transmission. The FSR of MRR is simply defined and calculated as[34]

$$\text{FSR} \approx \frac{\lambda^2}{n_g \cdot L}, \tag{3}$$

where λ is the resonant wavelength, n_g is the group index of the multimode waveguide, which can be obtained using the software COMSOL Multiphysics[35], and L is the perimeter of the MRR. Using the simulation software COMSOL Multiphysics, the calculated group refractive indices of TE$_0$ and TM$_0$ modes are 2.078 and 2.116 at 1550 nm, respectively. Therefore, the corresponding FSRs of the TE$_0$ and the TM$_0$ modes are 65.0 and 63.8 GHz, respectively. The measured transmission spectra of TE$_0$ and TM$_0$ modes are shown in Fig. 5(a). We can see that
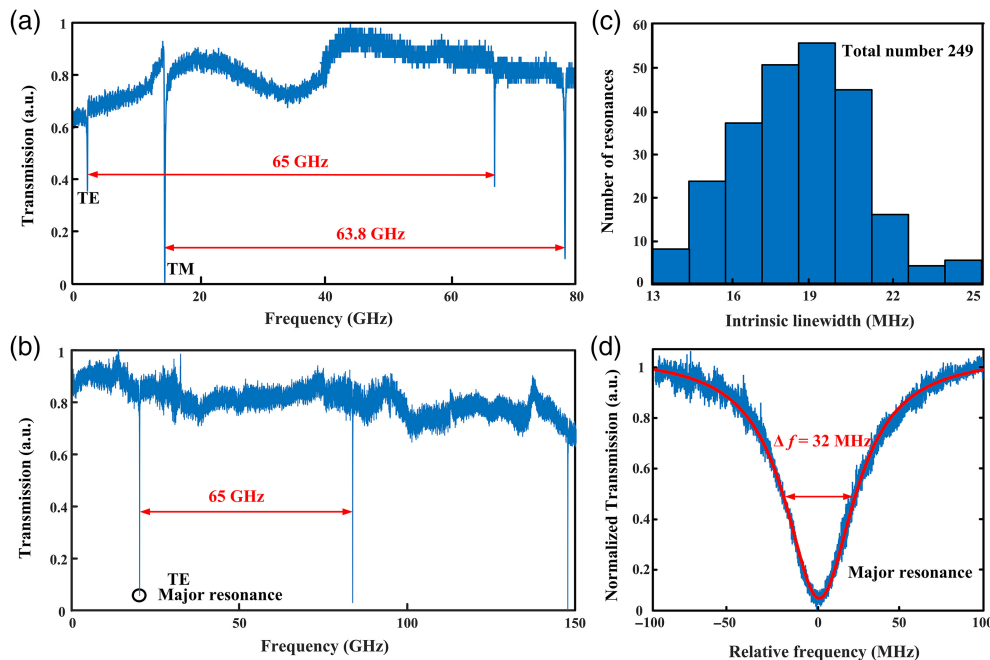
Fig. 5 Measured results of the MRR (height 0.8 μm × width 3.0 μm). (a) Measured transmission of the resonator when TE and TM mode resonances exist; (b) measured transmission spectrum when only TE mode resonance exists; (c) histogram of intrinsic linewidth of the MRRs; and (d) representative resonance with critical coupling.

the measured FSRs of TE_0 and TM_0 modes are 65.0 and 63.8 GHz, respectively, which agrees well with the theoretical results. When only the TE mode is required, we can adjust PC2 to make the SOP of input light to be aligned with the TE mode of the optical waveguide. From Fig. 5(b), it can be observed that there are no obvious resonant notches of higher-order modes, which proves that the designed MRRs can ensure adiabatic transmission for the fundamental mode.

To investigate the performance of the designed ultralow-loss Si_3N_4 multimode waveguide, we analyze the propagation loss of the waveguide beyond the single-mode regime by the following equations:[34]

$$Q_l = \frac{\lambda}{\Delta\lambda_{\text{FWHM}}} = \frac{\sqrt{t \cdot a} \cdot L \cdot \pi \cdot n_g}{(1 - t \cdot a) \cdot \lambda}, \qquad (4)$$

$$Q_i \approx \frac{2 \cdot \pi \cdot n_g}{\alpha \cdot \lambda}, \qquad (5)$$

where $\Delta\lambda_{\text{FWHM}}$ is the full width at half-maximum (FWHM) bandwidth of the MRR, t is the amplitude self-coupling coefficient of the bus waveguide, and a is the circumferential transmission coefficient, defined by $a = e^{-\alpha L/2}$. Here, α is the total loss in the MRR given by the sum of the scattering loss coefficient, radiation loss coefficient, and material loss. To have more statistics data to obtain the mean Q factor, Fig. 5(c) shows the intrinsic linewidths of the high-Q MRR with different coupling gaps and resonant wavelengths in the same wafer. According to the data fitting, the highest probable propagation loss α of the racetrack waveguide is about 3.3 dB/m, corresponding an estimated mean Q_i of 10.8×10^6. The highest probable intrinsic linewidth is between 18 and 20 MHz. A critically coupled resonance is shown in Fig. 5(d). The fitting curve indicates the FWHM is 32 MHz, which indicates that a Q_l of 6.3×10^6 and an intrinsic linewidth of 19.3 MHz ($Q_i = 10.3 \times 10^6$) are obtained.

Table 1 shows the comparison of recently reported ultrahigh Q Si_3N_4 resonators that have a Q_i higher than 10^7. The first three MRRs with a high Q factor are achieved by low-confinement Si_3N_4 waveguides and fabricated based on the ultralow-loss high-aspect-ratio (H-A-R) waveguide technology. It can be seen that all of the propagation losses are lower than 1 dB/m. However, all of the bending radii are very large and result in small FSRs, which restricts the application scenarios and is still not conducive to highly dense integration. Notably, devices based on high-confinement Si_3N_4 waveguides can overcome these challenges. Recently, there have been some reports of ultralow loss and high-confinement Si_3N_4 waveguides based on the traditional subtractive process and photonic Damascene process. However, the key to achieving low propagation loss all include introducing complex fabrication processes solely to minimize the scattering points at the waveguide interfaces, such as reflowing resist masks,[11,25,27] multipass lithography,[19,28] and optimizing the etch recipe.[10,19] These special fabrication techniques are nonstandard and incompatible with those standard processes in foundries. Notably, all of the reported high-Q Si_3N_4 MRRs are fabricated in laboratories, not for the MPW. Therefore, it is still greatly desired to achieve low-loss optical waveguides using the MPW, such as the standard LAT process. According to Ref. 37, the propagation loss of the fabricated Si_3N_4 waveguides based on LAT is ~20 dB/m. In contrast, using our proposed high multimode structure, the propagation loss is successfully reduced from 20 to 3.3 dB/m. Correspondingly, the fabricated racetrack resonator can achieve a mean Q_i as high as 10.8 million, and the FSR is as large as 65.0 GHz. The high-Q MRRs can be applied to many fields, such as optical soliton sources,[38] high-coherence/low-threshold Brillouin lasers,[39] optical frequency combs,[40] microwave photonic filters,[33] and optoelectronic oscillators.[41]

4 Conclusion

In summary, we have proposed and demonstrated an ultrahigh-Q MRR based on a high multimode waveguide. The waveguide width is optimized by the n-w model to reduce the scattering loss. A multimode waveguide-based DC is used to achieve adiabatic coupling for the fundamental mode and avoid higher-order mode excitation simultaneously. At the same time, the modified Euler multimode bending is employed to reduce the size and avoid exciting higher-order modes in the MRR simultaneously. Therefore, adiabatic coupling and adiabatic propagation for fundamental mode in multimode waveguides are achieved to ensure

Table 1 Comparison of reported high-Q resonators based on Si_3N_4.

Reference	$(W_{co} \times H)$ (μm)	Manufacturing process	Propagation loss (dB/m)	R/R_{eff} (mm)	Q (loaded)	Q (intrinsic)
2014[20]	11.0×0.04	H-A-R	0.32	9.65	4.2×10^7	8.1×10^7
2021[36]	8.0×0.10	H-A-R	0.1	0.95	1.50×10^8	2.2×10^8
2021[18]	11.0×0.04	H-A-R	0.06	11.787	2.11×10^8	4.22×10^8
2020[25]	2.1×0.95	Photonic Damascene process	1.4	2.3	—	2.3×10^7
2021[27]	2.2×0.95	Photonic Damascene process	1.0	—	—	3.0×10^7
2022[11]	2.2×0.95	Photonic Damascene process	2.4	—	—	1.3×10^7
2021[19]	2.6×0.73	Subtractive process	<1	0.147	—	3.18×10^7
2021[28]	1.9×0.74	Subtractive process	—	—	—	1.9×10^7
2023[10]	2.4×0.81	Subtractive process	2.6	—	—	1.4×10^7
2021[37]	0.8×0.8	Standard LAT process	20	0.5	—	2.0×10^6
This work	3.0×0.80	Standard LAT process	3.3	0.195	6.7×10^6	1.08×10^7

fundamental mode resonance. Thanks to the adiabatic DC and Euler bends, although the multimode waveguide width of the MRR is as wide as with 3 μm, only the fundamental mode is excited and transmitted in the MRR with ultralow loss, and higher-order modes are successfully suppressed. Compared with previous MRRs fabricated based on the same LAT process, our proposed high multimode waveguide can reduce the propagation loss from previous 20 to 3.3 dB/m. Correspondingly, the intrinsic Q is increased from previous reported 2 to 10.8 million. The high multimode design can be applied not only to Si_3N_4 but also to different material platforms. In principle, these high multimode structures can be further combined with sophisticated optimized fabrication processes to reduce propagation loss. The proposed approach opens wide opportunities for applications in microwave photonics, classical and quantum information processing, and ion sensing.

5 Appendix: Measuring the FSR of MRR

We perform a microwave photonic link, as shown in Fig. 4, to measure the ultrahigh-Q resonator transmission through VNA. As the bandwidths of PD and PM are both 40 GHz, the measuring range of the VNA is also set to be 40 GHz, which corresponds to a wavelength range of 0.32 at 1550 nm. Considering that the FSR of the ultrahigh-Q resonator is as large as ~65.0 GHz, the measured frequency response of the MPNF by VNA must be spliced. Taking Fig. 5(a) as an example, at first the wavelength of the TLS is adjusted to 1549.77 nm, and the OBPF is adjusted to eliminate the +1st-order sideband of the phase-modulated light. Then, the transmission of the microresonator from 1549.77 to 1550.09 nm can be measured by VNA. The next step is to adjust the wavelength of the TLS to 1550.09 nm, and the OBPF is also adjusted correspondingly to eliminate the +1st-order sideband of the phase-modulated light. Then, the transmission of the microresonator from 1550.09 to 1550.41 nm can be measured by VNA. Finally, the transmission spectra of TE_0 and TM_0 mode as shown in Fig. 5(a) can be obtained by splicing the two measured transmission spectra by VNA.

References

1. N. Margalit et al., "Perspective on the future of silicon photonics and electronics," *Appl. Phys. Lett.* **118**(22), 220501 (2021).
2. L. Zhang et al., "Ultrahigh-Q silicon racetrack resonators," *Photonics Res.* **8**(5), 684–689 (2020).
3. L. Zhang et al., "Ultralow-loss silicon photonics beyond the singlemode regime," *Laser Photonics Rev.* **16**(4), 2100292 (2022).
4. C. Calò et al., "Hybrid InP-SiN microring-resonator based tunable laser with high output power and narrow linewidth for high capacity coherent systems," in *Opt. Fiber Commun. Conf.*, California (2022).
5. Z. Wu et al., "Coexistence of multiple microcombs in monochromatically pumped Si_3N_4 microresonators," *Opt. Lett.* **47**(5), 1190–1193 (2022).
6. D. J. Moss et al., "New CMOS-compatible platforms based on silicon nitride and hydex for nonlinear optics," *Nat. Photonics* **7**(8), 597–607 (2013).
7. C. Xiang et al., "High-performance silicon photonics using heterogeneous integration," *IEEE J. Sel. Top. Quantum Electron.* **28**(3), 1–15 (2022).
8. A. L. Gaeta et al., "Photonic-chip-based frequency combs," *Nat. Photonics* **13**(3), 158–169 (2019).
9. F. Ferdous et al., "Spectral line-by-line pulse shaping of on-chip microresonator frequency combs," *Nat. Photonics* **5**(12), 770–776 (2011).
10. Z. Ye et al., "Foundry manufacturing of tight-confinement, dispersion-engineered, ultralow-loss silicon nitride photonic integrated circuits," *Photonics Res.* **11**(4), 558–568 (2023).
11. X. Ji et al., "Compact, spatial-mode-interaction-free, ultralow-loss, nonlinear photonic integrated circuits," *Commun. Phys.* **5**(1), 84 (2022).
12. A. M. Jones et al., "Ultra-low crosstalk, CMOS compatible waveguide crossings for densely integrated photonic interconnection networks," *Opt. Express* **21**(10), 12002–12013 (2013).
13. L. Chen et al., "Monolithically integrated 40-wavelength demultiplexer and photodetector array on silicon," *IEEE Photonics Technol. Lett.* **23**(13), 869–871 (2011).
14. L. Chen et al., "Monolithic silicon chip with 10 modulator channels at 25 Gbps and 100-GHz spacing," *Opt. Express* **19**(26), B946–951 (2011).
15. M. Sodagar et al., "High-efficiency and wideband interlayer grating couplers in multilayer $Si/SiO_2/SiN$ platform for 3D integration of optical functionalities," *Opt. Express* **22**(14), 16767–16777 (2014).
16. J. F. Bauters et al., "Silicon on ultra-low-loss waveguide photonic integration platform," *Opt. Express* **21**(1), 544–555 (2013).
17. M. Piels et al., "Low-loss silicon nitride AWG demultiplexer heterogeneously integrated with hybrid III–V/silicon photodetectors," *J. Lightwave Technol.* **32**(4), 817–823 (2014).
18. M. W. Puckett et al., "422 million intrinsic quality factor planar integrated all-waveguide resonator with sub-MHz linewidth," *Nat. Commun.* **12**(1), 934 (2021).
19. X. Ji et al., "Exploiting ultralow loss multimode waveguides for broadband frequency combs," *Laser Photonics Rev.* **15**, 2000353 (2020).
20. D. T. Spencer et al., "Integrated waveguide coupled Si_3N_4 resonators in the ultrahigh-Q regime," *Optica* **1**(3), 153–157 (2014).
21. X. Lu et al., "High-Q slow light and its localization in a photonic crystal microring," *Nat. Photonics* **16**(1), 66–71 (2022).
22. A. Misra et al., "Nonlinearity- and dispersion-less integrated optical time magnifier based on a high-Q SiN microring resonator," *Sci. Rep.* **9**(1), 14277–14287 (2019).
23. F. Vollmer and L. Yang, "Label-free detection with high-Q microcavities: a review of biosensing mechanisms for integrated devices," *Nanophotonics* **1**(3-4), 267–291 (2012).
24. M. H. P. Pfeiffer et al., "Ultra-smooth silicon nitride waveguides based on the Damascene reflow process: fabrication and loss origins," *Optica* **5**(7), 884–892 (2018).
25. J. Liu et al., "Photonic microwave generation in the X-and K-band using integrated soliton microcombs," *Nat. Photonics* **14**(8), 486–491 (2020).
26. J. Liu et al., "High-yield, wafer-scale fabrication of ultralow-loss, dispersion-engineered silicon nitride photonic circuits," in *Conf. Lasers and Electro-Opt. Eur. & Eur. Quantum Electron. Conf. (CLEO/Europe-EQEC)*, pp. 1–1 (2021).
27. J. Liu et al., "High-yield, wafer-scale fabrication of ultralow-loss, dispersion-engineered silicon nitride photonic circuits," *Nat. Commun.* **12**(1), 2236 (2021).
28. Z. Ye et al., "Integrated, ultra-compact high-Q silicon nitride microresonators for low-repetition-rate soliton microcombs," *Laser Photonics Rev.* **16**(3), 2100147 (2021).

29. X. Ji et al., "Ultra-low-loss on-chip resonators with sub-milliwatt parametric oscillation threshold," *Optica* **4**(6), 619–624 (2017).

30. Y. Li et al., "Large group delay and low loss optical delay line based on chirped waveguide Bragg gratings," *Opt. Express* **31**(3), 4630–4638 (2023).

31. D. Melati et al., "A unified approach for radiative losses and back-scattering in optical waveguides," *J. Opt.* **16**(5), 055502–055508 (2014).

32. M. Burla et al., "Ultra-high Q multimode waveguide ring resonators for microwave photonics signal processing," in *Int. Top. Meeting on Microwave Photonics (MWP)*, Paphos (2015).

33. X. Liu et al., "Silicon-on-insulator-based microwave photonic filter with narrowband and ultrahigh peak rejection," *Opt. Lett.* **43**(6), 1359–1362 (2018).

34. P. Rabiei et al., "Polymer micro-ring filters and modulators," *J. Lightwave Technol.* **20**(11), 1968–1975 (2002).

35. F. Peng et al., "Sensitivity prediction of multiturn fiber coil-based fiber-optic flexural disk seismometer via finite element method analysis," *J. Lightwave Technol.* **35**(18), 3870–3876 (2017).

36. W. Jin et al., "Hertz-linewidth semiconductor lasers using CMOS-ready ultra-high-Q microresonators," *Nat. Photonics* **15**, 346–353 (2021).

37. D. Chatzitheocharis et al., "Design of Vernier-ring reflectors in thick Si_3N_4 platform," *Proc. SPIE* **11689**, 116891W (2021).

38. N. G. Pavlov et al., "Narrow-linewidth lasing and soliton Kerr microcombs with ordinary laser diodes," *Nat. Photonics* **12**(11), 694–698 (2018).

39. K. Y. Yang et al., "Bridging ultrahigh-Q devices and photonic circuits," *Nat. Photonics* **12**(5), 297–302 (2018).

40. J. Liu et al., "Ultralow-power chip-based soliton microcombs for photonic integration," *Optica* **5**(10), 1347–1313 (2018).

41. L. Maleki, "The optoelectronic oscillator," *Nat. Photonics* **5**(12), 728–730 (2011).

Shuai Cui is currently pursuing his PhD at Wuhan National Laboratory for Optoelectronics, Huazhong University of Science and Technology (HUST), Wuhan, China. His current research interests include microwave signal processing and microwave signal generation.

Kaixiang Cao is currently pursuing his master's degree at Wuhan National Laboratory for Optoelectronics, HUST, Wuhan, China. His current research interests include microwave signal processing and microwave signal generation.

Zhao Pan is currently pursuing his master's degree at Wuhan National Laboratory for Optoelectronics, HUST, Wuhan, China. His current research interests include microwave signal processing and microwave signal generation.

Xiaoyan Gao is currently pursuing his doctoral degree at Wuhan National Laboratory for Optoelectronics, HUST, Wuhan, China. His current research interests include microwave signal processing and microwave signal generation.

Yuan Yu received a PhD in optoelectronic information engineering from the School of Optical and Electronic Information, HUST, Wuhan, China, in 2013. He is currently an associate professor at Wuhan National Laboratory for Optoelectronics and Institute of Optoelectronics Science and Engineering, HUST. His current research interests include microwave photonics and silicon-based integrated devices.

Xinliang Zhang received a PhD in physical electronics from HUST, Wuhan, China, in 2001. He is currently a professor at Wuhan National Laboratory for Optoelectronics and the School of Optical and Electronic Information, HUST. He is the author or coauthor of more than 300 journal and conference papers. His current research interests include InP-based and Si-based devices and integration for optical network, high-performance computing, and microwave photonics.